ARL-TR-9871 ● FEB 2024

Comparison of Hex and Tetra Skullcap with a User-Defined Skull Material Model

by Carolyn E Hampton and Caitlin M Weaver

NOTICES

Disclaimers

The findings in this report are not to be construed as an official Department of the Army position unless so designated by other authorized documents.

Citation of manufacturer's or trade names does not constitute an official endorsement or approval of the use thereof.

Destroy this report when it is no longer needed. Do not return it to the originator.

ARL-TR-9871 ● FEB 2024

Comparison of Hex and Tetra Skullcap with a User-Defined Skull Material Model

Carolyn E Hampton and Caitlin M Weaver
DEVCOM Army Research Laboratory

REPORT DOCUMENTATION PAGE

1. REPORT DATE	2. REPORT TYPE	3. DATES COVERED	
		START DATE	END DATE
February 2024	Technical Report	3/1/2023	1/5/2024

4. TITLE AND SUBTITLE
Comparison of Hex and Tetra Skullcap with a User-Defined Skull Material Model

5a. CONTRACT NUMBER	5b. GRANT NUMBER	5c. PROGRAM ELEMENT NUMBER
5d. PROJECT NUMBER	**5e. TASK NUMBER**	**5f. WORK UNIT NUMBER**

6. AUTHOR(S)
Carolyn E Hampton and Caitlin M Weaver

7. PERFORMING ORGANIZATION NAME(S) AND ADDRESS(ES)
DEVCOM Army Research Laboratory
ATTN: FCDD-RLA-TB
Aberdeen Proving Ground, MD 21005

8. PERFORMING ORGANIZATION REPORT NUMBER
ARL-TR-9871

9. SPONSORING/MONITORING AGENCY NAME(S) AND ADDRESS(ES)	10. SPONSOR/MONITOR'S ACRONYM(S)	11. SPONSOR/MONITOR'S REPORT NUMBER(S)

12. DISTRIBUTION/AVAILABILITY STATEMENT
DISTRIBUTION STATEMENT A. Approved for public release: distribution unlimited.

13. SUPPLEMENTARY NOTES
ORCID ID: Carolyn E Hampton, 0000-0002-7246-2488

14. ABSTRACT
The US Army Combat Capabilities Development Command Army Research Laboratory previously developed a vectorized user-defined material (VUMAT) model in Abaqus/Explicit to capture the failure behavior of human skull bone. Previous publications document the use of the VUMAT to simulate skullcap experiments and the VUMAT conversion from the Abaqus/complete Abaqus environment finite element (FE) solver to the LS-DYNA FE solver. This study further explored the skullcap simulation results by substituting a hexahedral mesh in place of the original tetrahedral mesh to address concerns about tetrahedra-induced noise in the force–time history and stress contours. First, homogeneous meshes were used and the tetra meshes were not subject to locking or excessive noise. Next, the skullcap meshes were compared with the element-specific bone volume fractions. Stresses and forces in these simulations were consistent in the tetrahedral meshes, and somewhat less consistent for the hexahedral meshes due to different contact and hourglass controls in Abaqus and LS-DYNA. Fracture patterns on the posterior skullcap surface in hexahedral meshes were limited by the preexisting mesh lines. These results suggested that the results with the tetrahedral mesh were not subject to unacceptable noise, produce superior fracture patterns, and therefore should be sufficient for future efforts to model skull impacts.

15. SUBJECT TERMS
biomechanics, finite element, simulation, bone, fracture, mesh, Abaqus, LS-DYNA, Mechanical Sciences, Terminal Effects

16. SECURITY CLASSIFICATION OF:			17. LIMITATION OF ABSTRACT	18. NUMBER OF PAGES
a. REPORT	b. ABSTRACT	C. THIS PAGE		
UNCLASSIFIED	UNCLASSIFIED	UNCLASSIFIED	UU	39

19a. NAME OF RESPONSIBLE PERSON	19b. PHONE NUMBER *(Include area code)*
Carolyn E Hampton	(540) 449-8801

STANDARD FORM 298 (REV. 5/2020)
Prescribed by ANSI Std. Z39.18

Contents

List of Figures

List of Tables

Acknowledgments

The authors would like to acknowledge Dr Richard Becker and Samantha Wozniak for providing technical review and feedback for this manuscript. The authors would also like to acknowledge additional team members Stephen Alexander, Timothy Baumer, Brian Fagan, Dr Michael Kleinberger, and Dr Tusit Weerasooriya for their work involving computational models of skull fracture that helped motivate this study.

1. Introduction

The US Army Combat Capabilities Development Command (DEVCOM) Army Research Laboratory (ARL) previously published a vectorized user-defined material (VUMAT A) model for use in Abaqus/Explicit to capture the behavior of human skull bone (Weerasooriya and Alexander 2021). An updated version was published later (VUMAT B) and is used in this study (Alexander et al. 2021). While there are many studies providing linear elastic and elastoplastic material properties for bone, this material model added some novel features: automatic scaling of the material and stress-based failure properties to account for the bone density, and a way to incorporate failure without directly deleting elements. These features allow a more realistic representation of the skull's natural density gradient versus the simplified three-layer structure (dense, hard inner and outer tables surrounding a soft, porous diploë layer), as well as a method to capture crack initiation and propagation. A previous study provided a case example of an excised skullcap subjected to quasistatic indentation until failure (Gunnarsson et al. 2021), which was successfully reproduced in the corresponding Abaqus finite element (FE) model.

Recently, this material model was converted to an LS-DYNA user-defined material to broaden the availability (Hampton et al. 2022). The skullcap case study was reproduced again in LS-DYNA to show that the results were the same between the two FE solvers. One of the limitations raised after completion of the study was potential issues with using a tetrahedral (tetra) mesh over a hexahedral (hex) mesh.

Tetra meshes are attractive due to the ease of generating meshes for complex geometry, but they can also be more computationally costly (more elements are needed to fill a given volume) than hex elements and can produce unrealistically stiff responses (Nagtegaal et al. 1974; Burkhart et al. 2013). Nagtegaal et al. (1974) attributed the stiff responses to volume locking that occurs with specific mesh layouts; however, this conclusion came from using an elastic-perfectly plastic material model for materials that are strictly incompressible at limit load (e.g., metals). This behavior could be avoided by implementing higher-order element types that have more degrees of freedom than constraints (e.g., 10-pt linear tetrahedron or quadratic hex). This current study examined mesh dependence with a bone material, which was both purely elastic and compressible. Furthermore, bone tends to fail like a brittle rather than a ductile material, which precludes an incompressible state. Therefore, the mesh type limitations addressed in Nagtegaal et al. (1974) and Burkhart et al. (2013) may not restrict the use of constant strain tetra elements to simulate bone.

Hex-only meshes are considered to result in a more accurate simulation output and lower computational cost (Schneider et al. 2022). However, it should be noted that these assertions are made based on results from subfailure simulations of simple structures (e.g., square and round beams). Creating a hex mesh for complex geometries (e.g., biological structures) is time consuming and can outweigh their computational efficiency, especially since computing power has become more affordable (Bourdin et al. 2007). Furthermore, several FE studies of bone have been performed to evaluate the computational response and accuracy of complex geometries modeled with tetra and hex meshes. When looking at loading on a proximal femur FE model, Ramos and Simões (2006) found that linear tetra elements resulted in stress, strain, and displacement outcomes that were closer to theoretical values calculated using a simplified femur geometry. Additional FE studies performed by this research group have shown that FE models of biological systems developed with linear tetra elements produce acceptable correlations (correlation coefficient = 0.77) for biological systems (Bola et al. 2021) when these models are developed using appropriate mesh quality and acceptance standards (Burkhart et al. 2013) and proper mesh convergence (Bola et al. 2016).

In addition to bone material, tetra elements also show reasonable performance when modeling soft tissue organ impacts (Bourdin et al. 2007), being 10% and 14% stiffer than the hex elements when modeled with linear viscoelastic and hyper-elastic viscous material types, respectively. Additionally, the force-deflection response of both element types fit within and showed less variation than the reported experimental results (Schmitt and Snedeker 2006). The linear hex mesh was shown to be the most computationally efficient of all the element mesh types used in this study. However, the linear hex mesh had hourglass problems, causing the linear tetra mesh to be more stable at higher-energy impacts.

The prior literature provides recommendations on element size and order but suggests that the choice between tetra or hex elements has trade-offs such that there was no clear best choice. Recommendations from the Schneider et al. (2022) study include the need for performers to evaluate the performance of different mesh types for specific target applications.

This study is intended to follow up the original works (Weerasooriya and Alexander 2021; Hampton et al. 2022) with an in-depth look at the effects of meshing the skullcap with linear hex elements and linear tetra elements in both the Abaqus and the LS-DYNA FE solvers. This will first be done with the bone as a uniform, perfectly homogenized material to separate mesh-related and bone volume fraction (BVF)-related effects and address concerns about excessive noise in tetra meshes. Following this, solutions in the form of force-displacement curves and fracture patterns obtained using the original element specific densities will be compared. More qualitative aspects such as the stress and strain fields developed in the test

specimens will also be explored. Finally, recommendations will be issued on when hex or tetra meshes would be more appropriate and which would be best suited for future work on dynamic skull impacts.

2. Methods

2.1 Skullcap FE Models

The skullcap impact simulations performed in this study all used the same model assembly, developed by Weerasooriya and Alexander (2021), consisting of three parts: 1) skullcap, 2) hemispherical indenter (D = 31.75 mm), and 3) support plate. The skullcap bottom surface was supported by a node-to-surface contact (hard pressure overclosure option) with the deformable aluminum plate. The aluminum plate was supported by through-thickness nodal single-point constraints at each of the four corners that prevented any translation and rotation. The full FE models with supporting plate, skullcap, and hemispherical indenter are shown in Fig. 1.

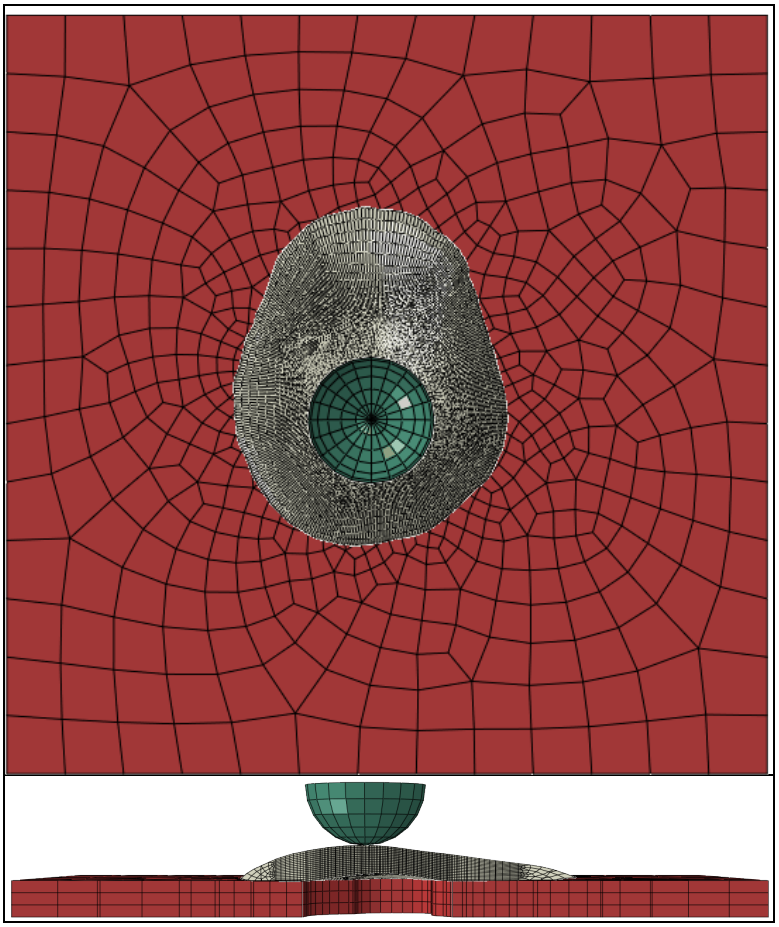

Fig. 1 FE model assembly of hex skullcap in top (top) and longitudinal cross-sectional views (bottom) in Abaqus

Two skullcap models were used, one with a tetra mesh containing 230,924 elements, and one with a hex mesh containing 201,144 elements (Fagan 2022). A view of the longitudinal cross-section of both mesh types is shown in Fig. 2. In both models, each element was assigned to one of 100 different BVF groups ranging between 0.005 to 0.995 via an automated script pairing elements to computed tomography (CT) voxels from a micro-CT scan of the specimen (Fagan 2022). The mode of maximum element length underneath the impactor was 0.965 and 0.451 mm for the tetra and hex meshes, respectively.

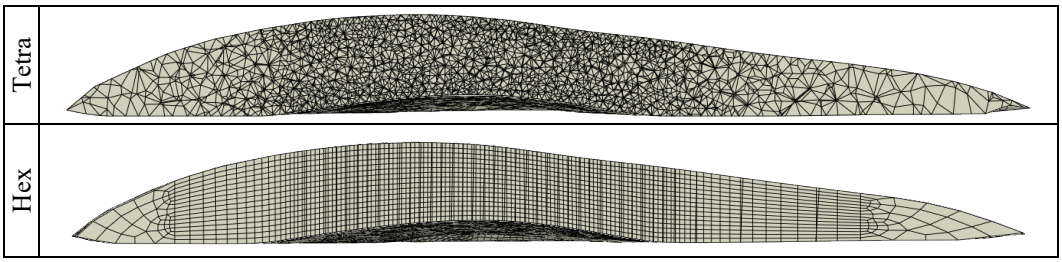

Fig. 2 Longitudinal cross-sectional views of the skullcap for tetra mesh (top) and hex mesh (bottom)

All impact simulations were performed by using a prescribed sine-like displacement of 3.3 mm over 10 ms, which was applied to the hemispherical rigid impactor, positioned over the apex of the skullcap. This motion is a piecewise fifth-order polynomial expression described in the Abaqus documentation for the amplitude keyword with the smooth option.

2.2 Homogenous VUMAT

To separate the influence of element type (hex vs. tetra) from the semi-random element BVFs, the tetra and hex mesh skullcaps were modified to use a single VUMAT material model with a BVF of 0.705. This value represented the transition from the cortical to diploë layer in the micro-CT voxels as reported by Alexander et al. (2021). The results were examined for changes in the crack pattern, stress and strain loading, and force versus displacement response.

2.3 Abaqus Simulations

Simulations for this portion of the study were performed using the Abaqus/CAE version 2020 explicit FE solver (Dassault Systèmes Simulia Corp) as outlined in Table 1. One set of simulations used the element specific (ES) implementation with 100 different VUMAT materials, while another set of simulations used the homogenous VUMAT. In total, four simulations were performed using the two skullcap meshes and the two versions of VUMAT. The hex and tetra skullcap were examined for von Mises stress, von Mises strain, and element states at 1 mm (3.90 ms), 2 mm (5.55 ms), 3 mm (7.60 ms), and 3.3 mm (10 ms) of displacement.

Indenter force and displacement and global energy balances were also collected at 1000 Hz.

Table 1 Abaqus simulations

Simulation	Mesh	Material
1	Hexahedral	ES
2		Homogeneous
3	Tetrahedral	ES
4		Homogeneous

2.4 LS-DYNA Simulations

Simulations that used the LS-DYNA explicit MPP FE solver (Ansys International, Inc) were run with version 12.0.0. Model preparation was done with HyperMesh 2017 (Altair Engineering, Inc) and postprocessing was automated with LS-PrePost 4.1 (Ansys International, Inc) scripting. The user-defined material model (Table 2) was implemented as previously described (Hampton et al. 2022). All of the simulations previously described in Table 1 were also run in LS-DYNA.

Table 2 LS-DYNA MAT_USER_DEFINED_MATERIAL card format for VUMAT material model. Implied units are mm-kg-ms.

MID	RO	MT	LMC	NHV	IORTHO	IBULK	IG
various	various	44	15	3	0	7	8
IVECT	**IFAIL**	**ITHERM**	**IHYPER**	**IEOS**	**LMCA**	**...**	**...**
1	...	...	...	...	...	...	...
BVF	**EXPN**	**EXPK**	...	...	...	**K**	**G**
various	1.603	2.0	...	...	...	various	various
REFRHO	**REFMOD**	**REFNU**	**REFSFC**	**REFSFT**	**REFSFS**	**REFSFR**	...
1.8E-6	3.0	0.3	0.175	0.2694	0.150	0.48	...

The spherical indenter from Abaqus was reproduced with a RIGIDWALL_GEOMETRIC_SPHERE_MOTION card of 31.75 mm diameter and was centered over the apex of the skullcap. It followed an identical sine-line path by implementing the Abaqus amplitude curve equation with the DEFINE_CURVE_FUNCTION keyword.

Translating the Abaqus surface interaction between the supporting plate and skullcap was not so straightforward. The best option for this study was a CONSTRAINT_NODE_TO_SURFACE contact. This changes the contact behavior from the LS-DYNA default penalty behavior, where a resisting force is applied to penetrating nodes proportional to penetration depth, to a constraint behavior, where the penetrating nodes are subject to whatever force is needed to prevent any penetration. This provided similar behavior to Abaqus.

LS-DYNA simulations with the hex-meshed skullcap used the stiffness-based form of Flanagan–Belytschko hourglass control (IHQ = 4) with default QM (0.1) to

suppress the hourglass modes associated with the under-integrated elements. Refer to Appendix A for more detail on the different hourglass control options. All LS-DYNA simulations also have time-step-based erosion enabled, which activates on elements falling to 10% of the original time step. This had minimal effect in previous simulations as the strain-rate-based erosion built into the VUMAT was more aggressive in eroding elements (Hampton et al. 2022).

3. Results

3.1 Homogeneous Simulations

3.1.1 Abaqus

The von Mises stress response of the skullcaps was evaluated in the Abaqus postprocessing solver in anterior, posterior, and longitudinal cross-sectional views (Figs. 3–5). A cut-off stress of 100 MPa was used to evaluate these simulation contours. Both mesh types showed similar von Mises responses in all three views for the homogeneous VUMAT. There is a concentration of stress shown on the outer and inner cortical region underneath the impact location. Visual differences between the hex and tetra skullcaps are shown in the anterior views at T = 5.55 and 7.60 ms (Fig. 3). The shape of the evolution of damage under the impact site shows similar bands of stress concentration; however, the shape of this damage is visually different. Differences are also shown in the longitudinal cross-sectional and posterior views at T = 5.55 and 7.60 ms (Fig. 5). The tetra skullcap displays a larger fracture/failure pattern on the outer cortical surface under the impactor. While damage under the impactor on the outer cortical region occurred with this material type, there were no linear fractures observed on the inner cortical surface (Fig. 4).

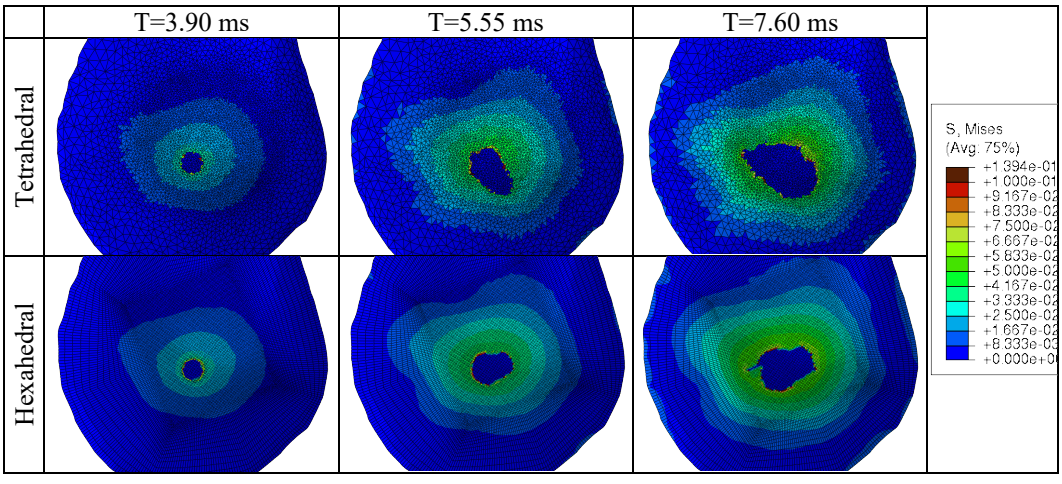

Fig. 3 Homogeneous Abaqus von Mises stress contours (GPa) projected onto the undeformed anterior (outer cortical) surface

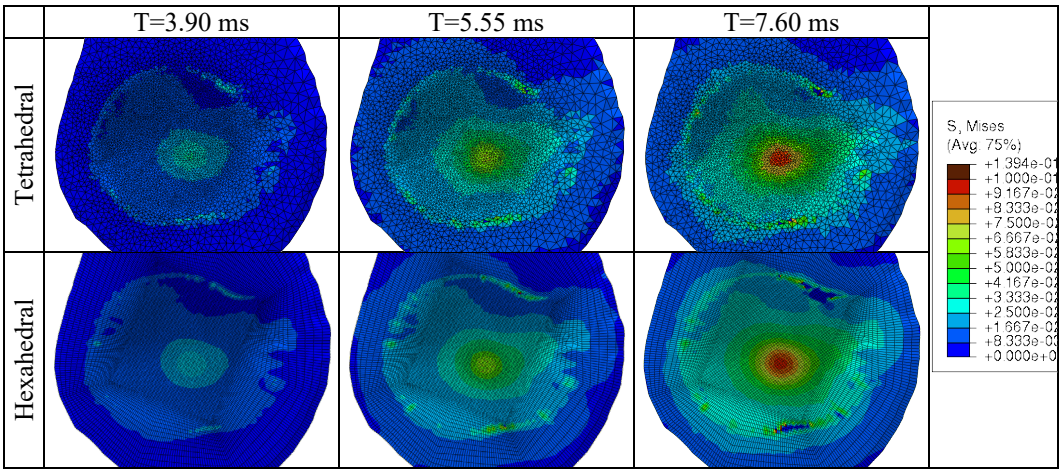

Fig. 4 Homogeneous Abaqus von Mises stress contours (GPa) projected onto the undeformed posterior (inner cortical) surface

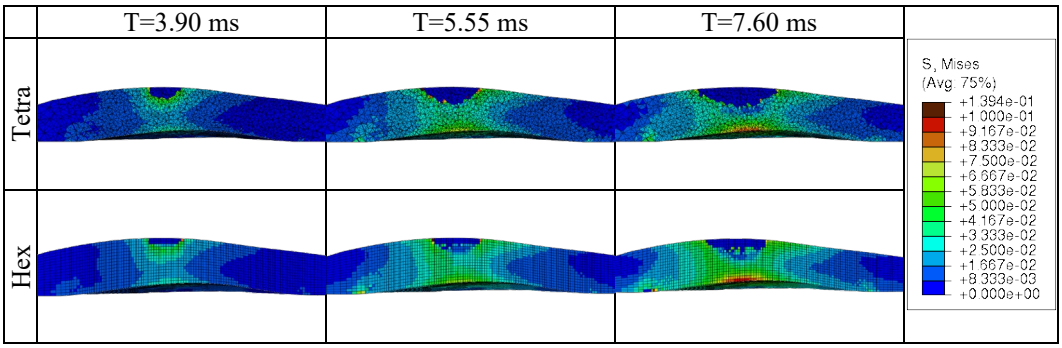

Fig. 5 Homogeneous Abaqus von Mises stress contours (GPa) projected onto the undeformed longitudinal cross section

3.1.2 LS-DYNA

LS-DYNA simulations with all elements sharing one homogenized BVF resulted in no fractures on the posterior surface of the skullcap (Fig. 6), and no damage to the elements in the middle region was sustained. This was consistent with the Abaqus results shown in Fig. 3, and the results were consistent between the hex and tetra meshes although the contour level boundaries were rougher in the tetra mesh. There was some compression-induced crush damage under the impactor for both meshes, which was also seen in Abaqus.

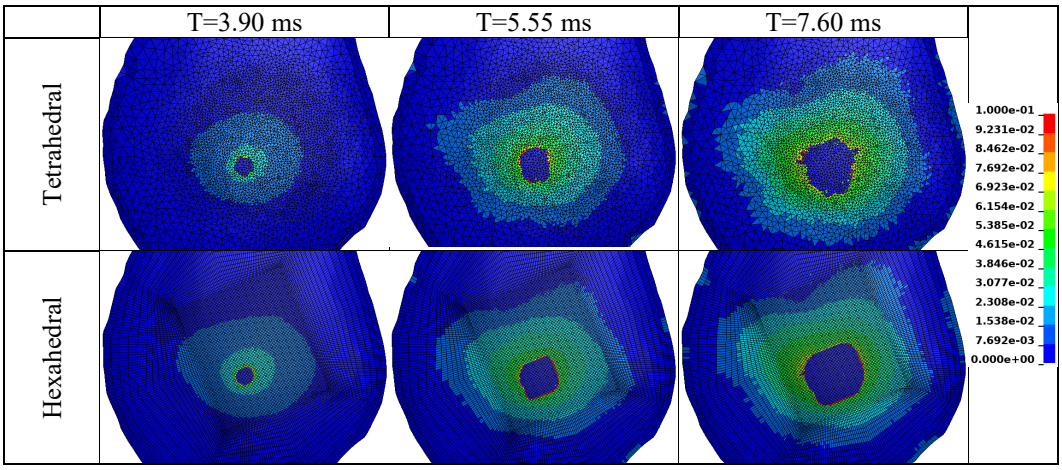

Fig. 6 Homogeneous LS-DYNA von Mises stress contours (GPa) projected onto the undeformed anterior surface

The von Mises stress contours on the posterior surface (Fig. 7) showed reasonable agreement between the hex and tetra meshes. These results are also in agreement with the Abaqus posterior contours shown in Fig. 4. The peripheral ring of elevated stresses from the plate contact and the failure of some elements in the ring were observed in both meshes, again consistent with the Abaqus results.

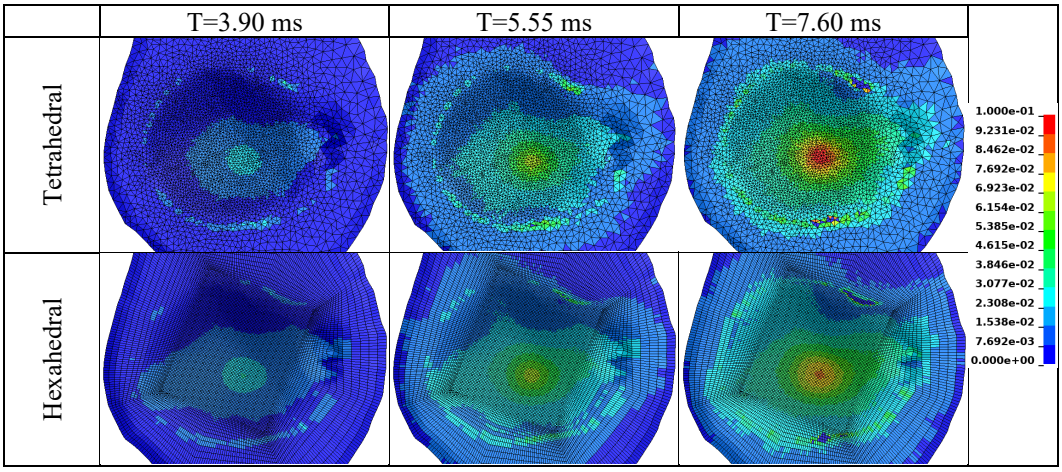

Fig. 7 Homogeneous LS-DYNA von Mises stress contours (GPa) projected onto undeformed posterior surface

Finally, the von Mises contours in the midline longitudinal cross section are shown in Fig. 8, and there was again a good agreement in the shape and magnitude between the tetra and hex meshes. These results are also the same as the Abaqus results in Fig. 5.

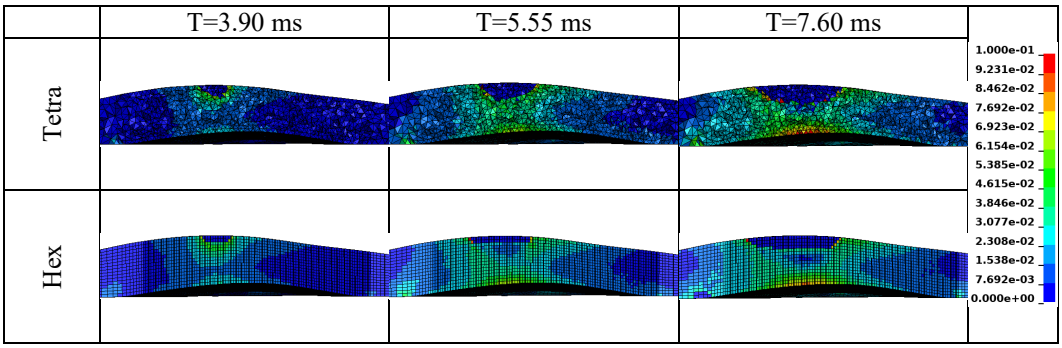

Fig. 8 Homogeneous LS-DYNA von Mises stress contours (GPa) projected onto the undeformed longitudinal cross section

3.1.3 Theoretical Stress Profile

The previous section on von Mises stress profile equivalences between both tetra and hex meshes and the Abaqus and LS-DYNA solvers did not address whether the stress patterns were realistic. Since these simulated skullcaps were a single homogenized material, the historical analytical solutions for the stresses inside a volume loaded by a parabolic indenter were relevant (Popov et al. 2019). In particular, the von Mises stress distributions can be calculated (Fig. 9). These solutions did not account for element erosion and non-infinite thickness in the FE models, so any comparisons must be made early in the simulation.

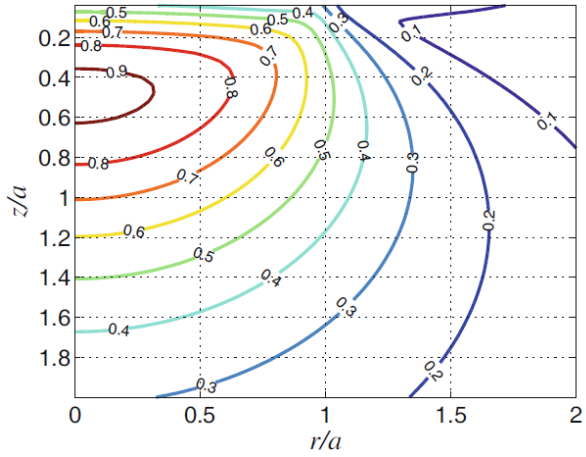

Fig. 9 Normalized contours of von Mises stress in a homogenous half-plane (reproduced from Popov et al. [2019] without modifications)

The stress distributions in the FE skullcaps at 2.2 ms are shown in Fig. 10, which was roughly the time at which the bending stresses on the posterior surface became visible but still before and any elements failed. At this time the deformations were minimal such that the skullcap was the most similar it could be to the theoretical half-space. The circular isolines and the existence of a focal point just underneath the surface match the theoretical predictions. The focal stresses developing on the posterior surface as the FE skullcaps were tensile as opposed to the mostly

compressive stresses on the anterior. There was a good agreement between the hex and tetra meshes, with the results from the tetra skullcap being a little noisier due to the unstructured mesh.

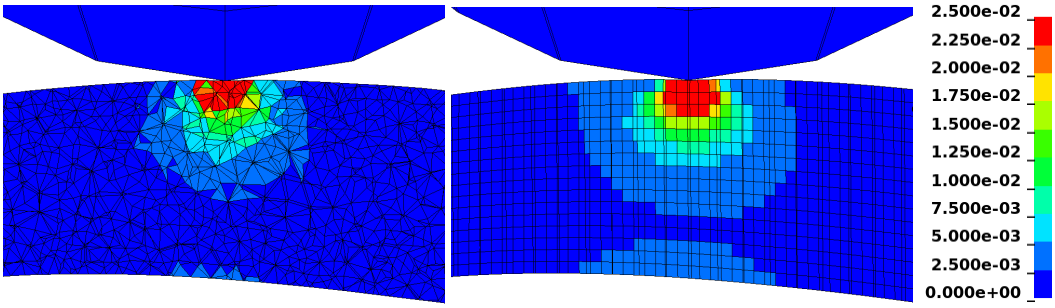

Fig. 10 Homogeneous LS-DYNA von Mises contours (GPa) in a longitudinal section cut 2.2 ms for tetra (left) and hex (right) meshes

The greatest von Mises stresses were found underneath the surface, which has interesting implications for both real bone and the ES skullcap simulations. Failure is often observed in the midplane of experimentally tested skull bone samples and is attributed to the lower density in the middle diploë layer. This region may be more vulnerable to damage than expected due to this stress-enhancing effect. This displaced focal stress is related to the indenter shape (i.e., parabaloid) and may be avoided in the future with other impactor shapes such as the cone (Popov et al. 2019). However, a truly perfect cone may be difficult to produce and maintain in physical experiments.

3.2 ES Simulations

The previous section showed that the tetra skullcap simulated stress distributions were noisier for the homogeneous material; however, this noise level was not quantified relative to that of the ES simulations. Additionally, the homogenous material model precluded the development of any microstructure-induced fracture patterns on the posterior surface. Since the initiation and propagation of fractures was a major feature of the VUMAT development, the simulations were repeated with the more complex element specific skullcap meshes that were used in previously published studies. Supplemental information on the energy balances, which can be used to gauge simulation stability and quality, are available in Appendix B.

3.2.1 Abaqus

The von Mises stress contours were evaluated in the anterior, posterior, and longitudinal cross-sectional views at 7.6 ms (Fig. 11). Both mesh types showed similar von Mises responses in all three views, with a concentration of stress shown on the outer and inner cortical region underneath the impact location. Initial failure

occurred on the outer cortical layer under the impactor while the stress increased on the inner cortical layer until fracture on this layer occurred. The most obvious visual difference between the hex and tetra skullcaps is shown in the longitudinal cross-sectional and posterior views. The tetra skullcap displayed a larger fracture/failure pattern on the inner cortical surface. As a result, the tensile bending stress on this surface was lower compared to the hex model due to the stress relief caused by the damage induced from this fracture/failure in the tetra model.

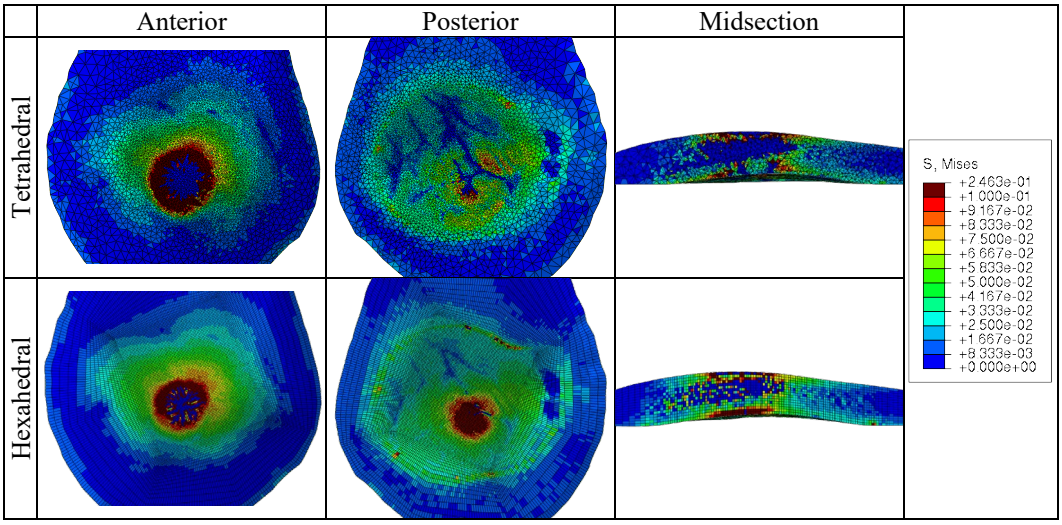

Fig. 11 Abaqus ES von Mises stress contours (GPa) at 7.60 ms projected onto the undeformed mesh

The element failures, which were based on the principal stresses, were evaluated at the simulation end time (T = 10 ms) using the same three orientations (Fig. 12). Both mesh types showed similar mechanisms of stress failure corresponding to failure in compression, tension, and shear. The pattern of fracture is different between the two mesh types. However, these differences are consistent with the propagation of fracture in hex meshes following the linear path of the mesh, which does not occur in unstructured tetra meshes.

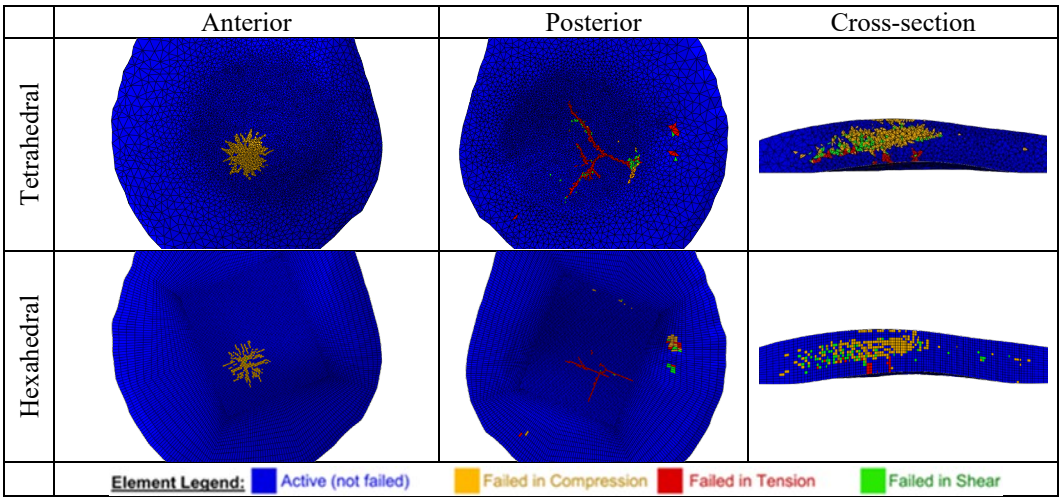

Fig. 12 Abaqus ES element states at 10 ms projected onto undeformed mesh

Comparing the von Mises stresses between the ES simulations (Fig. 11) and the homogeneous simulations (Figs. 6–8) revealed that the stress patterns were more irregular with the ES simulations. This suggested that a significant portion of the noise in the original tetra skullcap simulations could be attributed to the use of ES BVF values rather than the tetrahedral elements.

The force displacement (Fig. 13) shows critical failure in the hex skullcap at 3.68 kN (3.00-mm displacement). After this point, the reaction force drops off suddenly with increased displacement. The tetra model resulted in a nosier force versus displacement response, making it harder to determine the critical failure point. The tetra reaction force response produced two distinct peaks. Initial failure is determined to be the first peak (F = 3.04 kN, d = 2.48 mm) and critical failure was determined to be the second peak (F = 3.10 kN, d = 2.90 mm), after which the reaction force drops off suddenly with increased displacement.

Though the hex reaction force shows a small dip in force response at approximately 3.46 kN (2.71 mm), there is still a noticeable rise in force until the critical failure point is reached. Additionally, the hex skullcap hits critical failure at a higher force and displacement point. Both curves show that these element failures do not result in complete loss of skullcap integrity, since the skullcaps maintain a consistent force after 3 mm of displacement.

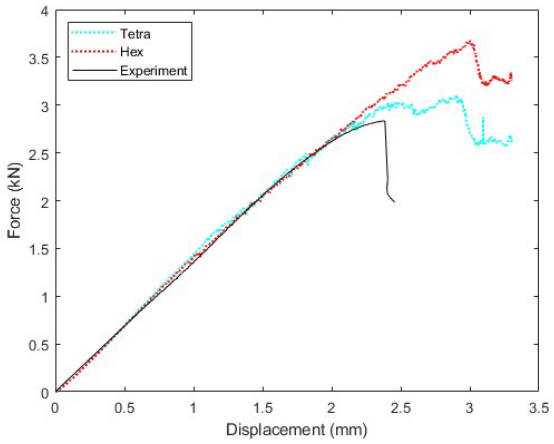

Fig. 13 Abaqus ES force-displacement curves for hex and tetra skullcaps

3.2.2 LS-DYNA

The von Mises stress contours are shown in Fig. 14 and can be cross-referenced against the Abaqus von Mises contours in Fig. 11. Both the tetra and hex skullcaps show a similar pattern of concentric rings of increasing stress on the anterior surface. On the posterior surface, the hexahedral skullcap showed a much higher tensile bending stress because the crack did not develop until 8.9 ms, which was also observed in the Abaqus hex skullcap. The cross-section view shows that the ES assignment of BVF resulted in the expected interior damage in the middle layer.

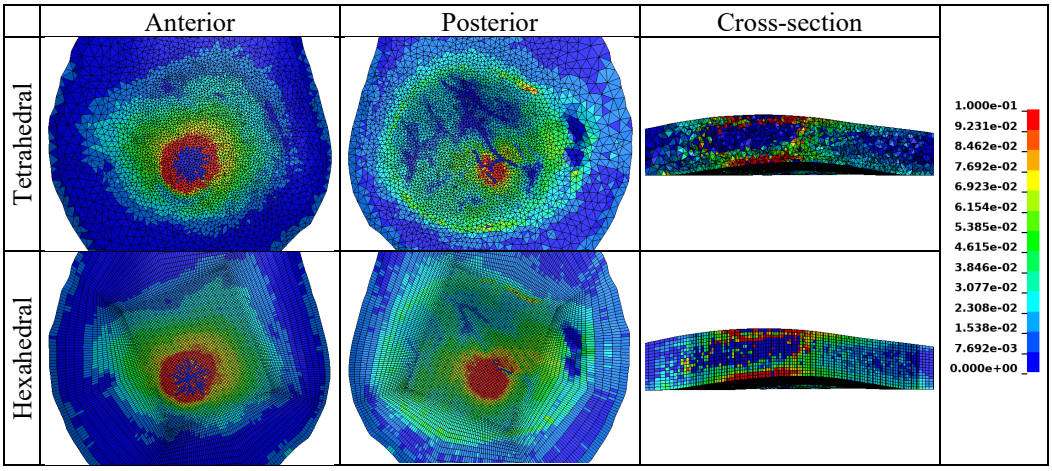

Fig. 14 LS-DYNA ES von Mises stress contours (GPa) at 7.6 ms projected onto the undeformed mesh

Figure 15 shows the element states at the end of each simulation, which can be compared to Fig. 12. By this time, cracks had developed on the posterior surface of both the tetra and hex skullcap. Both were compound linear cracks with many branches. The cross section revealed that many elements in the middle failed by compressive stresses. Cracks in the hex skullcap again tended to follow the mesh

lines more obviously than in the tetra mesh because of the regular rectangular layout of the mesh.

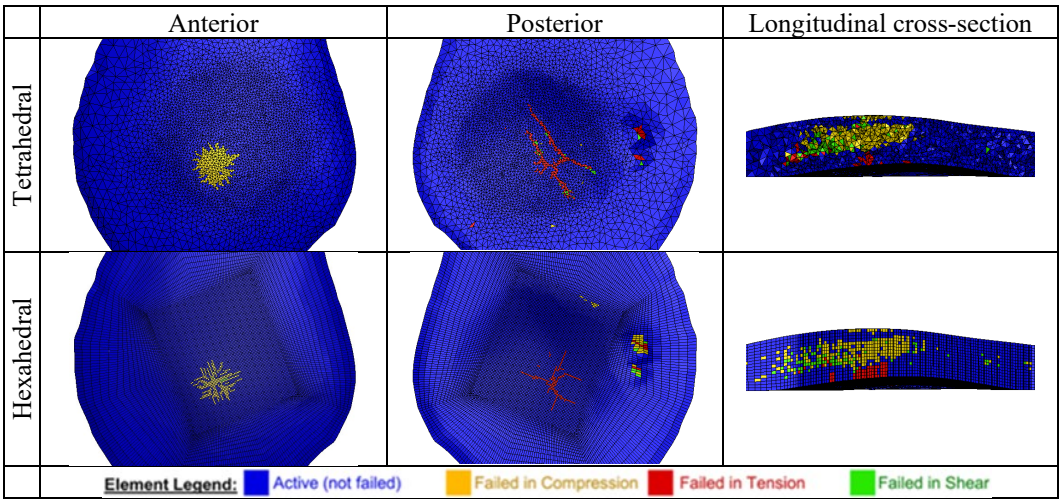

Fig. 15 LS-DYNA ES element state at 10 ms projected onto undeformed mesh

The force-displacement curves, which are often used to validate against experimental data, are shown in Fig. 16. The peak sustained forces were 3.30 kN in the tetra skullcap and 3.72 kN in the hex skullcap. These values occurred at 3.03 and 3.05 mm of indenter displacement, respectively. The hex skullcap exhibited a 13% greater peak force, which was attributed to the less uniform spatial stress distribution in the tetra skullcap leading to earlier element failures and initiation of the failure cascade. The VUMAT gradual damage mechanism ensured that the force history and stress distribution at failure were smooth, temporally. Noise in the signals was higher in the tetra results but was not as noticeable as the differences in the Von Mises stress contours.

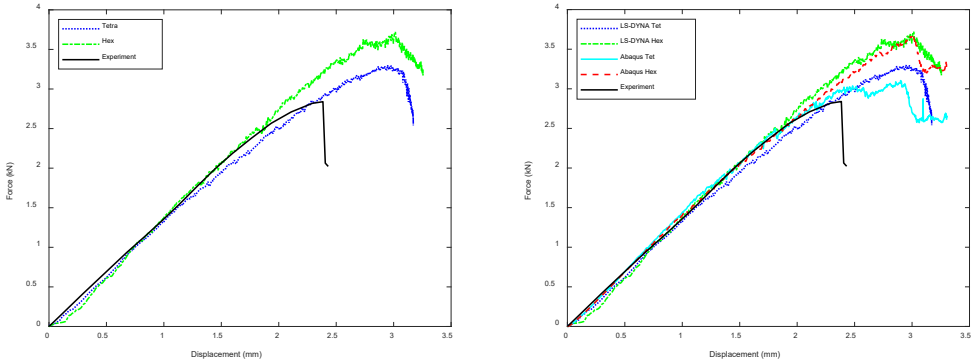

Fig. 16 LS-DYNA ES force-displacement curves for hex and tetra skullcaps (left), same curves plotted over the Abaqus ES force-displacement results (right)

These peak force results were comparable to those of Abaqus (Fig. 16), but the displacement needed to reach these values in the tetra skullcap was larger in LS-DYNA. These differences may have been introduced in the original conversion of

the user-defined material, where the displacement discrepancy and the lower stiffness in tetra was also observed in prior works (Hampton et al. 2022). The simulated solutions do not show failure at the same time or magnitude as the experiment, which was not yet a concern of this study as the material properties were not optimized to match the experimental results.

4. Discussion

The VUMAT was originally developed in Abaqus (Alexander et al. 2021) for use with tetra elements, which was then converted for use in LS-DYNA (Hampton et al. 2022). This study expanded upon that work by using Abaqus and LS-DYNA to evaluate differences in model response due to using hex elements. However, the use of ES BVF in the original studies was a potential confounding factor. Thus, a homogenous BVF skullcap was used to separate model response differences due to element type from BVF assignment.

While the tetra skullcaps are noisier for the homogenous material, this noise level is small compared to the stress variations produced by the ES volume fractions. The von Mises stresses for the homogenous simulations showed more consistent stress outcomes with cleaner contour level boundaries than the ES BVF simulations. This result also held when looking at tetra versus hex skullcap meshes and LS-DYNA versus Abaqus. The tetra skullcap displayed a larger fracture/failure pattern on the outer cortical surface under the impactor; however, the bands of stress concentrations were consistent between both mesh types on both cortical layers and the diploë. Cracking on the posterior surface was not observed in any homogenous simulation. The consistency in these results supports a conclusion that using tetra elements was not introducing harmful noise or volume locking effects.

For the ES simulations, both mesh types showed similar von Mises stress and strain failure responses in the material. However, there are noticeable differences in fracture patterns on the inner cortical surface of the skullcaps. Fracture patterns on the posterior (inner cortical) surface for both solvers were more extensive in the tetra skullcap. As a result, the stress relief on this surface was greater compared to the hex. Propagation of fracture in the hex meshes followed the linear path of the mesh, which did not occur in tetra meshes because of its unorganized alignment of elements. The differences in stress concentration were also detected in the force-displacement responses, which shows a higher force at failure for the hex model. The supplemental LS-DYNA simulations suggested that some of these differences could be attributed to hourglass control for hex meshes, which would be consistent with the challenges faced by Schmitt and Snedeker (2006). The VUMAT element damage algorithm, which depended on the simulation time step, also added some variability between solvers.

Figure 17 compares the fracture patterns observed in this study to the experimentally observed fracture pattern. In the original reports, the fracture was described as a "T" shaped pattern and many of the simulated fracture patterns exhibit this "T" joint, although all include additional cracks. However, the localization of the cracks was consistent. Cracks in the hex meshes showed a strong preference to follow the mesh lines, which was not observed in the tetra or the experimental specimen.

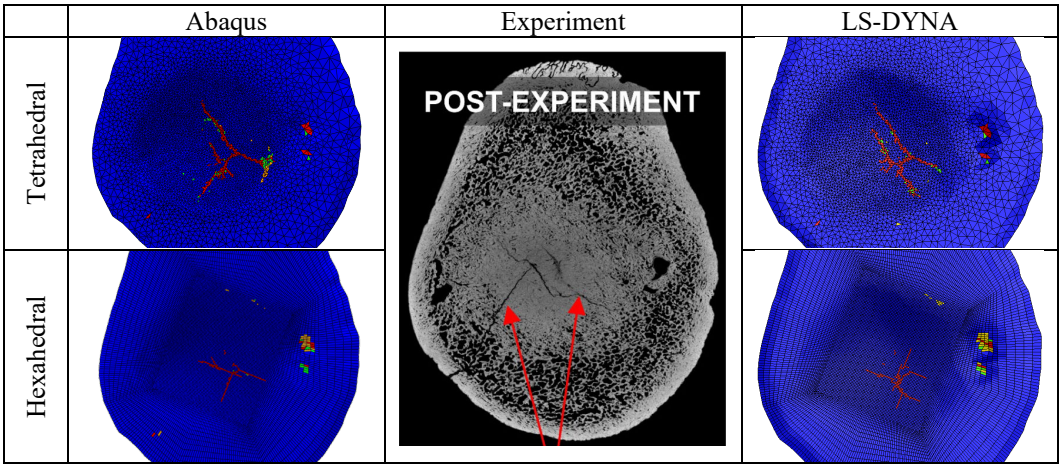

Fig. 17 Comparison of the simulated posterior surface fracture patterns with the experimentally observed fractures. Experimental fracture image (reproduced without modification from Alexander et al. [2021]); red arrows highlight the major cracks.

There were also differences in run time and termination status between the simulations. While all Abaqus simulations took longer than 8 h to complete, the hex simulations had run times that were noticeable shorter than the tetra simulations. Additionally, the homogeneous Abaqus tetra simulation took 33.3 h and ended with an error termination at T = 9.9 ms due to excessive incremental element rotation. Previous iterations of this simulation had earlier termination times. The termination time for this simulation was initially improved by applying mass scaling when the time step went below 5E-07 in Abaqus. Mass scaling helped extend the simulation progress to reach a displacement of 3.0 mm (T = 7.60 ms), so the results of this simulation were still able to be used for comparison with the hex simulation. Further updates were made to the model through the addition of distortion control, element deletion, and delete distorted element section controls, which improved the termination time from T = 8.529 ms to T = 9.9 ms.

Mass scaling and element deletion criteria were critical to maintaining the simulation time step at reasonable levels by helping with some element instabilities. Elements that switch to failed states have no strength in tension and no shear strength in compression, leading to severe distortion. For the Abaqus homogeneous material simulation, the primary mechanism of failure is compressive crushing failure, which contributed to these element instabilities and the need to implement

mass scaling and element deletion criteria. The mass scaling, incremental time step, and energy history outputs for this simulation were evaluated to determine the overall impact of these modification to the simulation output. Mass scaling was activated in this simulation at T = 5.93 ms, or after 2 mm of impact depth, which is in line with increased failure being observed in the model. After this simulation time and the activation of mass scaling, the incremental time step did not fall below the threshold value of 5E-07. The percent change in mass continues to rise to the end of the simulation with a final maximum percent change of 1.7% for the whole model.

An additional simulation was performed using element deletion criteria without the addition of mass scaling to determine if the effects to model energy outweighed the improvements in simulation computation time. The simulation without mass scaling did not show any significant changes to external, internal, frictional, kinetic, or hourglass energies but required twice as many licenses and nodes while also taking 96 h to reach termination. The homogeneous tetra energy plot discussed in Appendix B contains data from the final simulation run which utilized the mass scaling time step cut off and the element deletion criteria. Both simulations showed kinetic energy outputs slightly above zero with the value being slightly higher in the mass scaled simulation (KE = 0.17 J vs. 0.09 J).

The supplemental ES hourglass simulations for LS-DYNA also revealed that uncontrolled hourglassing added significant computational costs, both in time to complete and number of cycles. This did not affect Abaqus, as its internal hourglass handling was robust enough that this was not an issue but might have contributed to the differences in time to complete simulations. When hourglass was an issue in LS-DYNA, the best return on investment were in order 1) removing initial penetrations, 2) using constraint-based over penalty-based contacts, 3), using stiffness-based hourglass control, or 4) using the Cosserat hourglass, which nearly triples time to run simulations.

This study did not examine mesh sensitivities, particularly element size and aspect ratio, which can affect the propagation of stress and the performance of sliding contact algorithms. The element size was under the recommended element size of 1.5 mm used to simulate the shoulder assembly (Bola et al. 2016); however, this report went into the failure regime which might have stricter limits on the max element size. Table 3 summarizes the pros and cons of each element type for these skullcap simulations. Future work may address the differences from the experimental data that developed with changes to VUMAT and the applicability of the VUMAT to medium- and high-speed impacts.

Table 3 Summary of the pros and cons of tetra vs. hex meshes for the skullcap simulations

	Tetrahedral	Hexahedral
Pros	Easy to mesh	Structured mesh
	No hourglassing	Fewer elements
	Easier to capture nonlinear cracks	Elements cannot be volume locked
Cons	Unstructured mesh	Difficult to mesh
	More elements	Vulnerable to hourglass modes
	Mesh structure may cause volume locking	Cracks follow mesh lines

5. Conclusion

Simulations of a skullcap specimen were conducted to evaluate how the meshes (tetrahedral vs. hexahedral elements) would affect the results in two major FE solvers (LS-DYNA and Abaqus), and to determine how such results might be converged when they differ. The first part of this study used a homogenized skullcap, demonstrating that the tetra elements did not introduce too much noise for useable solutions, that the noise was lower than that introduced by the ES mesh, and that the hex mesh results could converge with the tetra mesh results. Follow-up studies also showed consistency in the interior stress profile and element failure behavior between the two meshes with some variability introduced by hourglass and contact options. While differences were observed between simulations with different mesh types, these findings support the use of tetra meshes when the geometries are complex and the results are sufficient for the purposes of this study.

6. References

Alexander SL, Baumer T, Fagan B, Weerasooriya T. Hybrid experimental modeling computational (HEMC) skullcap simulation: elemental to layer simplification and application to microstructural stochasticity. DEVCOM Army Research Laboratory (US); 2021. Report No.: ARL-TR-9296.

Bola AM, Ramos A, Simões JA. Sensitivity analysis for finite element modeling of humeral bone and cartilage. Biomater Biomech Bioeng. 2016;3(2). http://dx.doi.org/10.12989/bme.2016.3.2.071.

Bola M, Simões J, Ramos A. Finite element model validation based on an experimental model of the intact shoulder. Med Eng Phys. 2021;87. https://doi.org/10.1016/j.medengphy.2020.11.004.

Bourdin X, Trosseille X, Petite P, Beillas P. Comparison of tetrahedral and hexahedral meshes for organ finite element modeling: an application to kidney impact. 20th International Technical Conference on the Enhanced Safety of Vehicles (ESV); 2007. National Highway Traffic Safety Administration. 07–0424.

Burkhart TA, Andrews DM, Dunning CE. Finite element modeling mesh quality, energy balance and validation methods: a review with recommendations associated with the modeling of bone tissue. J Biomech. 2013;46. https://doi.org/10.1016/j.jbiomech.2013.03.022.

Fagan BT. A script for mapping computed tomography (CT) values to a finite element (FE) mesh for use with a biofidelic skull bone material model. DEVCOM Army Research Laboratory (US); 2022. Report No.: ARL-MR-1065.

Gunnarsson CA, Alexander SL, Weerasooriya T. Mechanical response and fracture of human skull to blunt indentation loading. DEVCOM Army Research Laboratory (US); 2021. Report No.: ARL-TR-9142.

Hampton CE, Alexander SA, Weerasooriya T. Conversion of a user-defined bone material model from Abaqus to LS-DYNA. DEVCOM Army Research Laboratory (US); 2022. Report No.: ARL-TR-9594.

Nagtegaal JC, Parks DM, Rice JR. On numerically accurate solutions in the fully plastic range. Comp Meth Appl Mech Eng. 1974;4:153–177.

Popov VL, Hess M, Willert E. Normal contact without adhesion in handbook of contact mechanics. Springer-Verlag GmbH; 2019. https://doi.org/10.1007/978-3-662-58709-6.

Ramos A, Simões JA. Tetrahedral versus hexahedral finite elements in numerical modelling of the proximal femur. Med Eng Phys. 2006;28. https://doi.org/10.1016/j.medengphy.2005.12.006.

Schmitt K. Snedeker JG. Analysis of the biomechanical response of kidneys under blunt impact. Traffic Injury Prev. 2006;7(2):171–181. https://doi.org/10.1080/15389580500482021.

Schneider T, Hu Y, Gao X, Dumas J, Zorin D, Panozzo D. A large-scale comparison of tetrahedral and hexahedral elements for solving elliptic PDEs with the finite element method. ACM Trans Graph. 2022;41(3), Art. No. 23. https://doi.org/10.1145/3508372.

Smith M. ABAQUS/standard user's manual, version 6.9. Dassault Systèmes Simulia Corp; 2009.

Weerasooriya T, Alexander S. Mechanism and microstructure based concept to predict skull fracture using a hybrid-experimental-modeling-computational approach. J Mech Behav Biomed Mater. 2021;121(104599). https://doi.org/10.1016/j.jmbbm.2021.104599.

Appendix A. Hourglass Controls

This report briefly described the hourglass options used to stabilize the hexahedral (hex) skullcap simulations without going into the details of why that particular formulation was chosen. Without an appropriate hourglass control, the skullcap tended to exhibit an unrealistic ring pattern of failed elements such as shown in Fig. A-1. There was interplay with the contact chosen for the skullcap–plate interactions. The indenter force and fracture patterns would change when not using the constrained node to surface contact in this report.

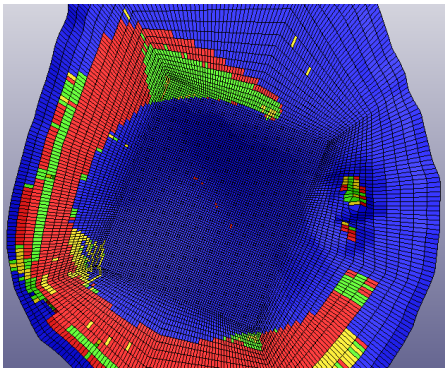

Fig. A-1 Example of an unrealistic posterior surface failure pattern in an LS-DYNA hex skullcap simulation using viscous hourglass (IHQ = 1) and a contact with initial penetration. Contour shows element state at 10 ms.

Table A-1 shows the full list of hourglass type (IHQ) and coefficient (QM) options considered for the element specific hex skullcap. No additional tetrahedral (tetra) simulations were run since tetra elements do not exhibit hourglass modes. No additional Abaqus simulations were listed since the results did not change with the limited options available.

Table A-1 LS-DYNA settings used for the supplemental hex hourglass type simulations

Simulation name	Hourglass type (IHQ)	Hourglass coefficient (QM)
Hg01	1	0.1
Hg02	2	0.1
Hg03	3	0.1
Hg04	4	0.1
Hg05	5	0.1
Hg06	6	1.0
Hg09	9	0.1
Hg10	10	0.1

The resulting posterior surface fracture patterns are shown in Fig A-2. The viscous-based hourglasses (types 0–3) developed some internal damage in the middle layer but no external cracks. Hourglass energy accounted for 43% of the total energy at best, and sometimes up to 93%. The classical hourglass element shapes were subtle without increasing the deformation scale factor; the increased number of cycles and

real time needed to simulate were more noticeable. However, these viscous hourglass controls did not add any artificial stiffness (compare Fig. A-3 vs. Fig. 16).

The stiffness hourglass types (types 4–6) showed much better energy control and developed the expected fracture patterns. The fracture patterns and force-displacement curves (Fig. A-3) were consistent between all the different stiffness options. All of the stiffness-based hourglass types added stiffness to the skullcap. The increased stiffness was 1.53 kN/mm over the 1–2 ms window, which was 15% higher than observed in the tetra skullcap (1.33 kN/mm).

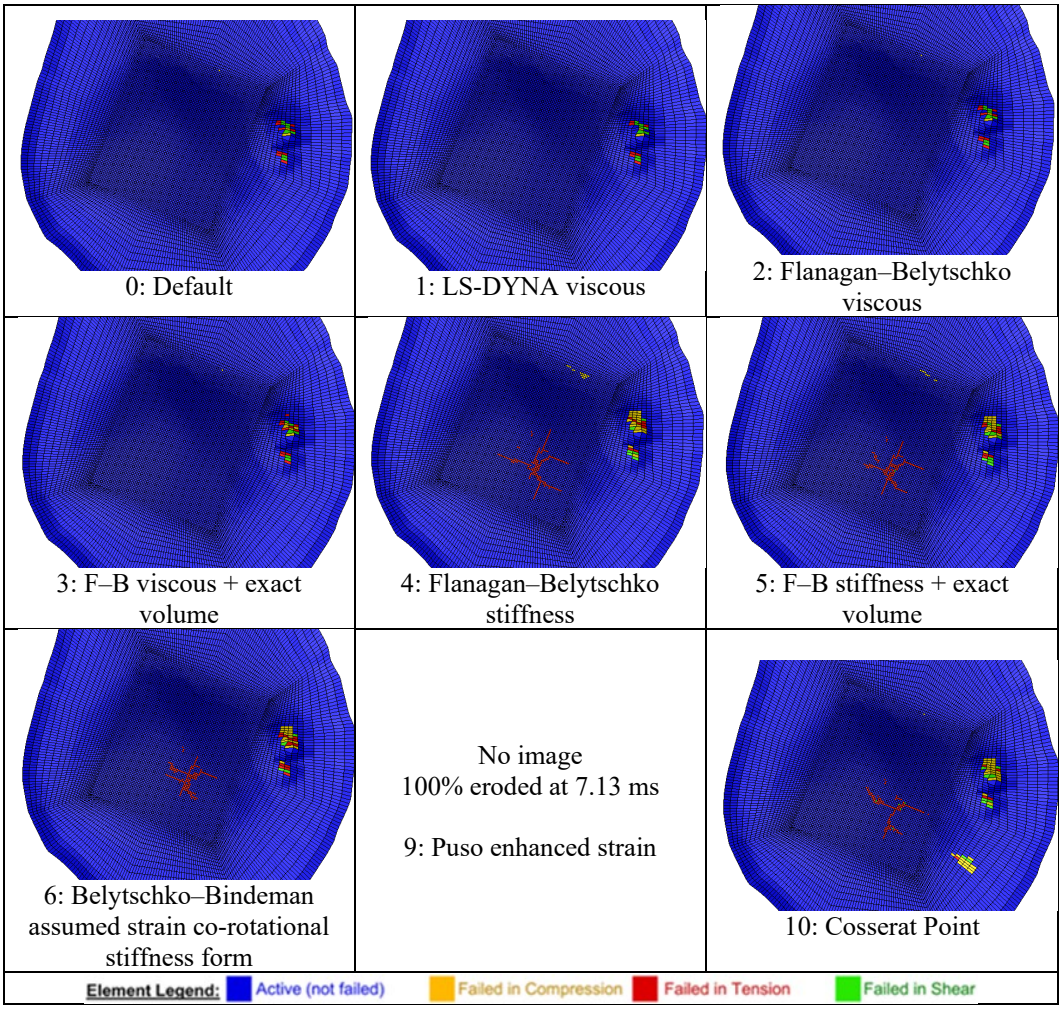

Fig. A-2 LS-DYNA element specific (ES) simulation element state contours on the posterior surface of the hex skullcap for various hourglass types. All images are projected onto the undeformed mesh and were taken at 10 ms.

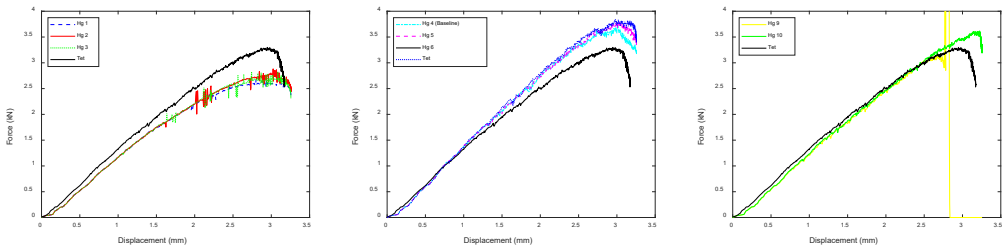

Fig. A-3 LS-DYNA ES hex skullcap force-displacement curves for viscous (left), stiffness (middle), and other (right) hourglass types. Solid black line shows the tetra results for comparison.

Of the two remaining hourglass options, only the Cosserat Point hourglass (Fig. A-2: 10) was stable enough to obtain a solution. The fracture pattern with this option was slightly different but reasonable, and negligible artificial stiffness was introduced (1.38 kN/mm). However, the time needed to simulate with this hourglass option were roughly 2.5× as long as with the stiffness hourglass (Fig. A-2: 4).

Appendix B. Energy Analysis

This appendix reviews the global energy balances associated with each simulation. Simulations that exhibited smooth energy traces and total energy sums that matched the amount of externally applied energy to move the indenter were valuable indicators of a robust and stable simulation. Similarly, sudden jumps in energies, large negative energies, or large amounts of energies sunk into artificial hourglass and damping were valuable in identifying the existence and location of a problem.

B.1 Abaqus

Figure B-1 compares the simulation global energies. The viscous dissipation accounts for the majority of the energy not shown in the figure. The energy types shown in these figures are not all the energy outputs available from these Abaqus simulations but were chosen for a more direct comparison to the available energy outputs in LS-DYNA (Figure B-2). While there were differences between peak values, both meshes were dominated by internal and external energies. A noticeable difference was the artificial strain, that is, hourglass energy response. For both tetrahedral (tetra) skullcap simulations, this energy was near zero throughout the whole simulation. However, with the element specific (ES) hexahedral (hex) skullcap, the hourglass energy began to rise at approximately 2.5 ms until it hit a peak of 1.26 J. For the homogeneous hex case, the hourglass response had a similar start time rise with a peak energy of 1.52 J. Additionally, there were substantial accumulations of frictional energy not seen in the ES cases. While the hex simulations showed similar internal and external energy responses, the homogeneous tetra simulation shows noticeably different curve rise times and peak values compared to the ES simulation.

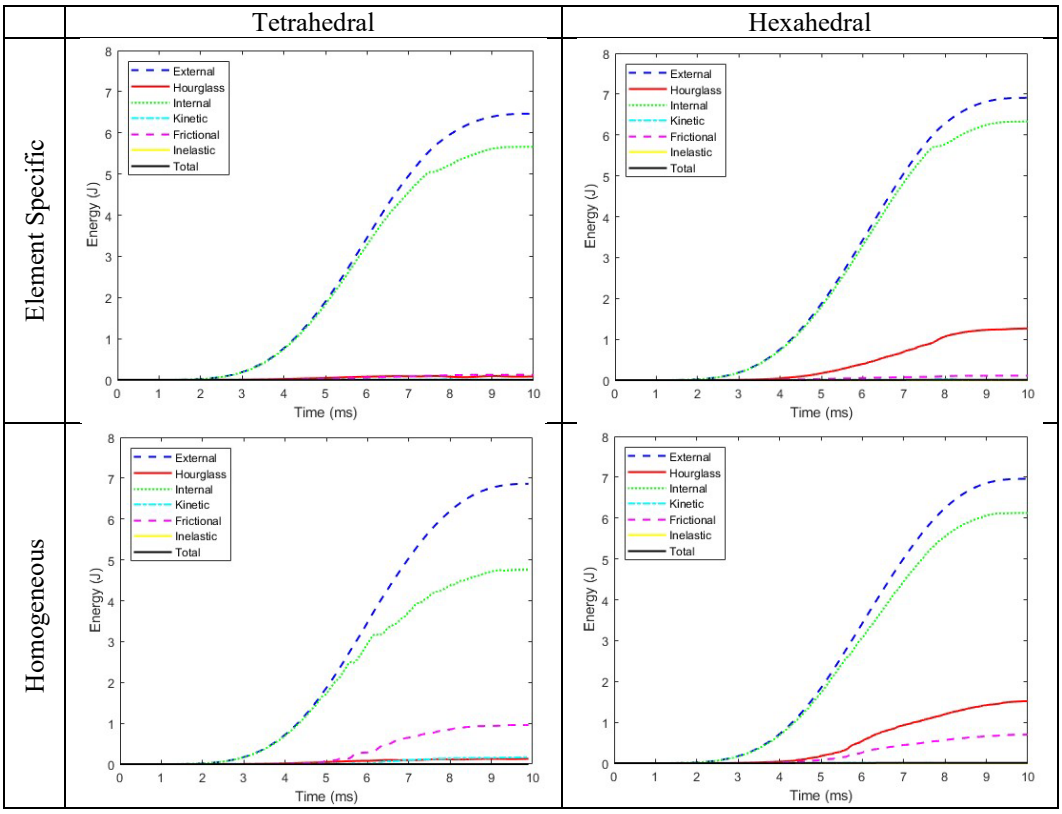

Fig. B-1 Abaqus global energies

The total energy, equal to the external work subtracted from the sum of the internal, viscous, frictional, and kinetic energies, resulted in a total energy of zero, which was indicative of a stable simulation. Based off the energy calculations provided in the Abaqus user's manual (Smith 2009), the hourglass energy is included in the internal energy calculation. The ES material model shows a difference in internal and external energy as element failure/fracture occurs in the model. The change in internal energy can be attributed to the failure response of elements written in the vectorized user-defined material. Elements that meet the conditions for failure in a previous time step are treated as a quasi-fluid material in future time steps and only carry compressive stress (Weerasooriya and Alexander 2021).

B.2 LS-DYNA

Figure B-2 shows the energy balances. Note that LS-DYNA reported energy differently than Abaqus. Here, the total energy was the sum of all other energies excluding the external energy and was expected to track with the external energy. Frictional energies were split by source, with the sliding interface and rigid wall frictional energies being split into the Sliding and Rigidwall categories, respectively.

For the ES simulations, the total and external energies were nonconstant and roughly equal throughout all simulations as expected with a prescribed motion boundary condition. The maximum energies were 6.1 and 6.8 J for the tetra and hex skullcaps, respectively. The 0.77 J increase in energy in the hex skullcap was an artifact of the hourglass controls (89% of increased energy) that made the simulation stable. The remaining increase was kinetic energy in failed elements (9%) and contact energy (2%). The total energies with a viscous-based hourglass control were closer to the tetra skullcap energies (not shown) but have massive hourglassing and were more likely to terminate early with errors. In both, the friction, kinetic, and hourglass energies were much lower than the internal energy. These results were consistent with the Abaqus results in Fig. B-1.

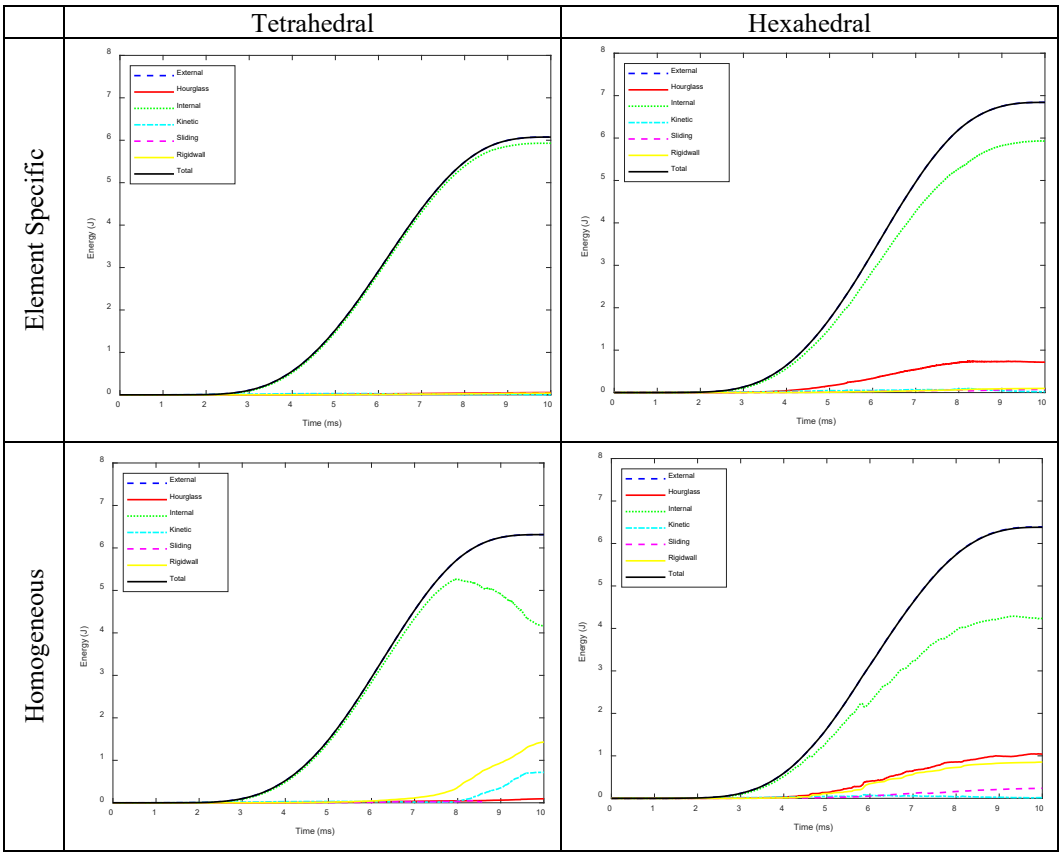

Fig. B-2 LS-DYNA global energies

Figure B-2 also reviews the energies associated with homogenous simulations. These simulations were more consistent in the total energy, with 6.3 J in the tetra skullcap and 6.4 J in the hex skullcap as few elements change to failed states. These simulations have more rigid wall energy generated by friction and displacement of nodes under the impactor since the middle layer was not able to erode, which in turn prohibited flexion. The homogenous tetra simulation showed some substantial kinetic energies as well. This was also seen in Abaqus to a lesser degree and was indicative that the simulation was approaching an error termination even though no visual signs were observed.

List of Symbols, Abbreviations, and Acronyms

ARL	Army Research Laboratory
BVF	bone volume fraction
CAE	complete Abaqus environment
CT	computed tomography
D	indenter diameter
d	simulation displacement
DEVCOM	US Army Combat Capabilities Development Command
ES	element specific
F	simulation force
FE	finite element
hex	hexahedral
IHQ	LS-DYNA hourglass type
QM	LS-DYNA hourglass coefficient
T	simulation time
tetra	tetrahedral
VUMAT	vectorized user-defined material

1 (PDF) DEFENSE TECHNICAL INFORMATION CTR DTIC OCA

1 (PDF) DEVCOM ARL FCDD RLB CI TECH LIB

1 (PDF) DEVCOM DAC K LOFTIS

30 (PDF) DEVCOM ARL FCDD RLA CB R BECKER P GILLICH C HOPPEL FCDD RLA HC A EIDSMORE A DAGRO FCDD RLA T R FRANCART FCDD RLA TB S ALEXANDER R BANTON T BAUMER B FAGAN A GOERTZ A GUNNARSSON R GUPTA C HAMPTON M KLEINBERGER R KARGUS D KRAYTERMAN E MATHEIS J MCDONALD P MCKEE K RAFAELS S SATAPATHY M TEGTMEYER C WEAVER T WEERASOORIYA S WOZNIAK T ZHANG FCDD RLA TD R DONEY FCDD RLB J ZABINSKI FCDD RLR EM AD BROWN